LANGMUIR

pubs.acs.org/Langmuir
Article

Improving Rare-Earth Mineral Separation with Insights from Molecular Recognition: Functionalized Hydroxamic Acid Adsorption onto Bastnäsite and Calcite

Robert C. Chapleski, Jr., Azhad U. Chowdhury, Anna K. Wanhala, Luke D. Gibson, Dīāna Stamberga, Santa Jansone-Popova, Robert L. Sacci, Harry M. Meyer, III, Andrew G. Stack, Vera Bocharova,* Benjamin Doughty,* and Vyacheslav S. Bryantsev*

Cite This: *Langmuir* 2022, 38, 5439−5453

Read Online

ACCESS | Metrics & More | Article Recommendations | Supporting Information

ABSTRACT: Enhancing the separation of rare-earth elements (REEs) from gangue materials in mined ores requires an understanding of the fundamental interactions driving the adsorption of collector ligands onto mineral interfaces. In this work, we examine five functionalized hydroxamic acid ligands as potential collectors for the REE-containing bastnäsite mineral in froth flotation using density functional theory calculations and a suite of surface-sensitive analytical spectroscopies. These include vibrational sum frequency generation, attenuated total reflectance Fourier transform infrared, Raman, and X-ray photoelectron spectroscopies. Differences in the chemical makeup of these ligands on well-defined bastnäsite and calcite surfaces allow for a systematic relationship connecting the structure to adsorption activity to be framed in the context of interfacial molecular recognition. We show how the intramolecular hydrogen bonding of adsorbed ligands requires the inclusion of explicit water solvent molecules to correctly map energetic and structural trends measured by experiments. We anticipate that the results and insights from this work will motivate and inform the design of improved flotation collectors for REE ores.

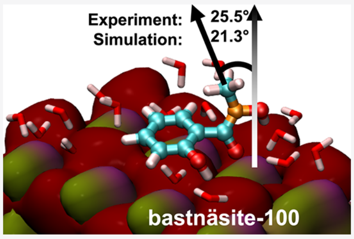

■ INTRODUCTION

The exceptional electronic and magnetic properties of elements across the lanthanide series provide a correspondingly unique set of materials and functions based on these elements that have become essential to a range of applications, including magnets in computer equipment and wind turbines, industrial catalysts, glare-resistant glass, and polishing media.[1−4] Though largely comprising the class of so-called rare-earth elements (REEs), these metals are not so rare in the Earth's crust; cerium, for example, is about as abundant, on average, as copper.[5,6] Conversely, the "rarity" of this class of elements lies in the fact that they are not typically found in concentrated deposits as frequently as other materials. Among the few REE deposits currently in production are the Bayan Obo mine in China and Mountain Pass in the United States of America, both of which are rich in bastnäsite, (Ce, La)-FCO_3.[1,7−11]

Further contributing to the perceived rarity of the REEs is the difficulty in separating desirable REE content from unwanted, or gangue, mineral content ubiquitous in mined ores. Bastnäsite, for example, is interspersed with calcite ($CaCO_3$) in ores. The similar structures of the REE-containing bastnäsite and the gangue calcite, both of which incorporate carbonate anions, render the separation of these two minerals challenging. REE beneficiation, or separation of desired mineral content from gangue, is partly achieved through the process of froth flotation. In this process, the ore is crushed and ground into fine particles and mixed into a slurry containing water and collector agents, among other compounds. Collector agents are generally surfactant-like species that differentially adsorb onto REE minerals and increase their hydrophobicity. When air is subsequently bubbled through the slurry, the collector-adsorbed REE mineral adheres to the bubbles and floats to the top of the flotation cell. The froth contains a higher concentration, or grade, of REE than the starting ore and is skimmed from the top of the cell and further refined in subsequent processing steps.

Hydroxamic acids—amides wherein an amino hydrogen is substituted for a hydroxyl group—are currently being explored and practically applied as collectors in froth flotation. Following their initial use in transition-metal separation,[12−14] hydroxamic acids have shown efficacy in REE beneficiation.[15−19] The potential for hydroxamic acids[20,21] collectors is based on the high recovery, 60−72%, of REE content from mined ores relative to other collectors. However, the need for

Received: December 23, 2021
Revised: March 24, 2022
Published: April 20, 2022

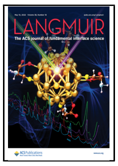

https://doi.org/10.1021/acs.langmuir.1c03422
Langmuir 2022, 38, 5439−5453

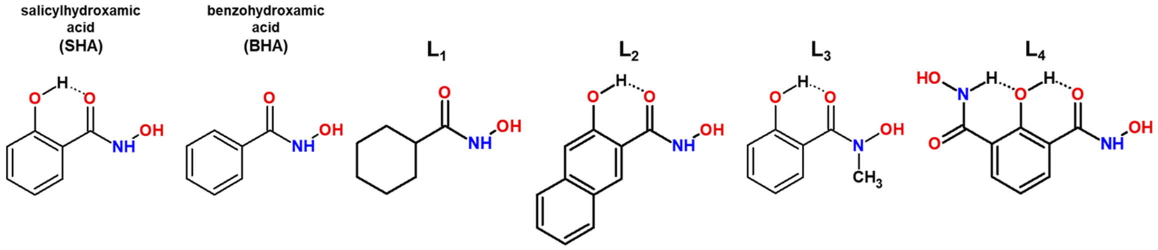

Figure 1. Chemical structures of ligands discussed in this work. Intramolecular hydrogen bonds present in lowest-energy structures in implicit water solvent are shown with dashed lines.

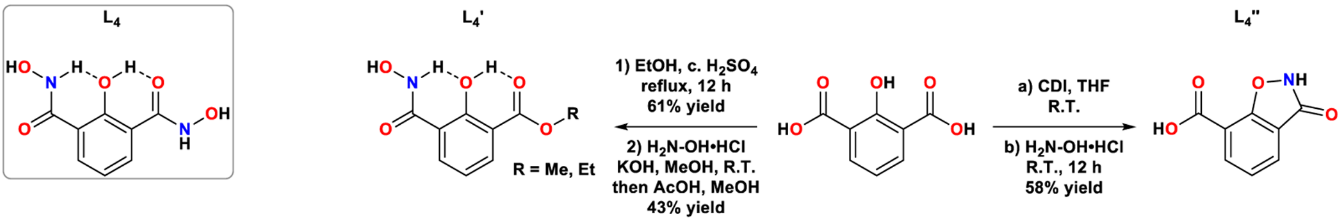

Figure 2. Attempted synthesis of L_4 and synthesis of mono-hydroxamic acid L_4' and mono-carboxylic acid L_4''.

more selective collectors is shown while comparing absolute yields to that of sulfide.[22]

New collector compounds have historically been selected through intuition, trial-and-error, or anecdotal means and guided by experimental trends and observations. Along these lines, experimental studies have provided insights into conditions that lead to the best REE recovery. These approaches typically focus on flotation performance with respect to temperature, pH, and collector concentration and describe chelative chemosorption of collector ligands on REE minerals and weaker interactions with gangue minerals.[23−32] More recently, studies have begun to enlist surface sensitive spectroscopies, such as vibrational sum frequency generation (vSFG)[19] and X-ray photoelectron spectroscopy (XPS)[24,33,34] measurements, contributing molecular-scale insights into binding between sites on the mineral surface and atoms in the hydroxamic acid moiety.

In the forefront of developing new collectors, researchers are extensively considering molecular-scale phenomena as guides.[35] A fundamental understanding of specific interactions among individual collector molecules, adsorption sites on mineral surfaces, and solvent molecules can provide detailed insights into the mechanisms driving effective REE beneficiation via froth flotation. This fundamental approach is included within the more general molecular recognition paradigm, wherein the structure of a ligand is differentially aligned, spatially and electronically,[26] in relation to the structures of different mineral surfaces, leading to different interactions, and therefore recognition, of the surfaces by the ligand molecule.[36−39] Revealing such fundamental descriptions of molecular-scale recognition phenomena requires surface-sensitive experimental methods and accurate theoretical approaches. Thus, recent work[19,40−42] has focused on understanding and developing new collectors for bastnäsite flotation by enlisting a combination of specialized spectroscopic and density functional theory (DFT) methods supported by macroscale experimental data to demonstrate feasibility.

Beginning with an elucidation of the most stable surfaces of bastnäsite, Srinivasan et al.[40,41] described the orientation of water molecules and associated interactions with these surfaces using DFT, X-ray diffraction, and adsorption calorimetry methods. A comparison of water adsorption on the most stable bastnäsite and calcite surfaces informed on differences related to interatomic spacing on the mineral surfaces. The authors suggest that collector molecules would bind differently on bastnäsite than on calcite due to the fact that functional units are less compact in the former mineral than in the latter. This difference could contribute to strain in collector molecules upon adsorption on either surface and provide a means for recognition. A follow-up study by Wanhala et al.[18] probed the adsorption of an alkyl hydroxamic acid onto bastnäsite as a function of collector coverage. DFT and attenuated total reflectance Fourier transform infrared (ATR-FTIR) spectroscopy revealed coverage-dependent differences in hydroxamic-acid-moiety interactions with the surface. Monodentate ligand binding modes were implicated at low concentrations, whereas bidentate binding was found at high concentrations. vSFG spectroscopy afforded additional insights near the surface by revealing the orientations of the alkyl chains at different coverages. We have since extended this approach to a detailed investigation of salicylhydroxamic acid (SHA) adsorption onto the most stable surfaces of bastnäsite and calcite using DFT, ATR-FTIR, vSFG, and Raman spectroscopy.[42] Considering SHA alongside two ligands with reduced functionality—benzohydroxamic acid (BHA), which lacks a phenolic hydroxyl group, and salicylic acid, which lacks a hydroxamic acid group—allowed us to probe the contribution of individual functional groups to adsorption on each surface. We found that the hydroxamic acid moiety is responsible for strong collector adsorption on both mineral surfaces, while the phenolic group anchors SHA to the bastnäsite surface, causing a surface-parallel orientation at a wide range of ligand coverages. Closer ionic spacing in calcite leads to a more surface-normal orientation of SHA on the gangue-mineral surface.

In the present work, we examined five functionalized hydroxamic acid ligands as potential collectors for REE-containing bastnäsite mineral in froth flotation. These ligands, shown in Figures 1 and 2, are functional derivatives of SHA and were chosen to describe the relationship between adsorption activity and ligand chemistry and structure. The functional group substitutions represented by these ligands provide insights into the role of the ringed moiety in the adsorption onto both mineral surfaces which has not been explored to our knowledge but should impact the spatial footprint and strain in the ligand taken at the interface. In this regard, both L_1 and L_2 have recently shown promise in bastnäsite microflotation studies.[31,34,43,44] Similarly, for a new ligand L_3, wherein the amino hydrogen in SHA is substituted for a methyl group and a new ligand L_4 with a second hydroxamic acid moiety in the meta position, we gain important insights into the role of intramolecular hydrogen bonding and each added functional group on adsorption, leading to the future design of more effective flotation agents. Finally, due to the difficult synthesis of L_4, another new ligand, L_4', was studied, which substitutes a methyl ester for one of the hydroxamic acid groups in L_4. This ligand exhibits similar intramolecular hydrogen bonding to L_4 and still provides an additional functional group for surface interaction compared to SHA. Furthermore, we consider the adsorption of hydroxamic acid ligands in the presence and absence of explicit solvent molecules in DFT simulations, revealing the role of specific water−ligand interactions on adsorption onto bastnäsite and calcite mineral surfaces. We anticipate that this work, a synergy of DFT, vSFG, ATR-FTIR, Raman, and XPS approaches, will provide further insights into the molecular recognition of hydroxamic acids onto bastnäsite and calcite surfaces and ultimately lead to the design of more effective collectors for REE beneficiation.

■ METHODS

Computational Methods. Periodic density functional theory calculations were performed using the Vienna ab initio software package (VASP),[45−48] versions 5.4.4 and 6.2.1. Valence electronic states were expanded in a basis of plane waves, and the core−valence interactions were described using the projector-augmented wave method.[49,50] For all calculations, the PBE functional[51,52] was employed along with Grimme's D3 dispersion correction[53] and an energy cutoff of 600 eV unless otherwise noted. Electronic convergence was achieved when the energy difference between consecutive self-consistent-field steps was less than 10^{-5} eV. All structures reported in this work result from geometry optimizations, and geometric convergence was achieved when the force on each atom was less than 10^{-2} eV/Å. All atomic coordinates were permitted to relax during geometry optimization. The energies of all optimized geometries, including slabs and free ligands, were modified at the single point by a dipole correction along the surface-normal axis (or in all three Cartesian dimensions for species in the absence of mineral surfaces), as well as a solvation energy correction calculated using VASPsol[54,55] to model implicit water solvent. All adsorption energies reported in this work using eqs 1 and 2 thus reflect these modified electronic energies.

Mineral surfaces were constructed as 2 × 2 × 1 supercells of the most stable surfaces of both bastnäsite and calcite, resulting in a seven-layer slab of $CeFCO_3$ for bastnäsite-$[10\bar{1}0]$ and a five-layer $CaCO_3$ slab for calcite. Cell parameters along the interfacial planes were taken from the optimized bulk structures[41] and kept fixed during geometry optimization. Cerium was exclusively chosen as the REE in our DFT calculations for bastnäsite, as Ce is the most abundant light REE found in mined bastnäsite ores.[1] A 20 Å vacuum layer was added to each surface to prevent interactions of adjacent periodic slab images normal to the surface.

To one surface of each mineral slab, a single ligand molecule was added, contributing to a conformational search of at least seven unique orientations for each ligand−mineral system. Each conformational search considered multiple surface-bound rotamers, protonation states, and ligand orientations relative to the surface normal. Gas-phase ligands L_1, L_3, and L_4 (in the absence of mineral surfaces) were optimized in a periodic 18 × 18 × 18 Å unit cell, while L_2 and L_4' (Figure 2) employed a 21 × 21 × 21 Å cell. Possible rotamers of a free ligand were sampled to identify the most stable ligand conformation in implicit solvent. The unit cells chosen for all ligands resulted in well converged electronic energies with respect to cell size.

Adsorption energies were calculated according to eq 1

$$E_{\text{ads}} = E_{(\text{ligand-surface})} - (E_{\text{ligand}} + E_{\text{surface}}) \quad (1)$$

where E_{ads} is the adsorption energy, $E_{\text{ligand-surface}}$ is the energy of the system containing the ligand adsorbed onto the mineral surface, E_{ligand} is the energy of the ligand in the absence of the surface, and E_{surface} is the energy of the mineral surface in the absence of any ligand.

The lowest-energy structures resulting from conformational searches of L_3 and L_4, as well as SHA and BHA[42] were used as starting points for explicit solvation studies. Sixteen water molecules (i.e., two water molecules per surface metal cation) were explicitly added to each ligand-bound mineral surface, and three consecutive simulated annealing cycles using ab initio molecular dynamics (AIMD) were initiated, during which all atomic coordinates were permitted to evolve. Each cycle consisted of four stages of at least 1000 steps of 1 fs each. First, the temperature was ramped from 300 to 600 K, followed by equilibration at 600 K, then a ramp from 600 to 300 K, and finally equilibration at 300 K. All AIMD runs enlisted an energy cutoff of 400 eV, a 1 × 1 × 1 *k*-point mesh, and the Nosé-Hoover thermostat[56−59] with the frequency of the temperature oscillations defined by SMASS = 0.32. The final structure of each cycle was then geometry optimized and electronic energies were subsequently dipole- and solvent-corrected in the manner described above for systems without explicit water molecules. Following optimization after each annealing cycle, at least three further attempts to minimize low-energy geometries were made for each system by manually moving individual water molecules to maximize interactions. Adsorption energies of ligands on explicitly solvated mineral surfaces were calculated according to eq 2

$$E_{\text{ads}} = E_{(\text{ligand-16H}_2\text{O-surface})} - (E_{\text{ligand}} + E_{(16\text{H}_2\text{O-surface})}) \quad (2)$$

where $E_{\text{ligand-16H}_2\text{O-surface}}$ refers to explicitly solvated minerals with hydroxamic acid ligand adsorbed, and $E_{16\text{H}_2\text{O-surface}}$ is the energy of the explicitly solvated mineral surface in the absence of the ligand.

To assist in the assignment of the vibrational modes measured by ATR-FTIR, molecular calculations were performed for ligands L_3 and L_4' using the Gaussian 16 Revision A.03 software package.[60] Each ligand was considered in the deprotonated form with two explicit water molecules and in a bidentate complex with Ce^{3+} explicitly hydrated with seven water molecules following the methodology described in our previous work.[18]

Synthesis. The hydroxamic acids L_1−L_3 were prepared according to the literature[61−63] procedures (as detailed in the Supporting Information). The attempts to prepare di-hydroxamic acid L_4 were unsuccessful. Using two different synthesis methods, the mono-hydroxamic acid L_4' and mono-carboxylic acid L_4'' were isolated instead. In the first synthesis method, the 2-hydroxyisophthalic acid was converted into di-ethyl ester which was then reacted with excess of free-base hydroxylamine/KOH solution in methanol. This resulted in the isolation of a mixture of two products: methyl 2-hydroxy-3-(hydroxycarbamoyl)benzoate and ethyl 2-hydroxy-3-(hydroxycarbamoyl)benzoate in a 1.3:1 ratio, respectively (L_4' in Figure 2). In the second synthesis method, the 1,1′-carbonyldiimidazole (CDI)-mediated coupling reaction between 2-hydroxyisophthalic acid and hydroxylamine hydrochloride resulted in the formation of ligand L_4'' where the in situ formed hydroxamic acid underwent intramolecular cyclization.[64] Among the two obtained products, compound L_4' most closely resembles the target substrate L_4; therefore, it was used in the computational and experimental studies described below.

Vibrational Sum Frequency Generation. vSFG experiments were carried out on a home-built spectrometer described in detail elsewhere.[65,66] Briefly the output of an amplified femtosecond laser

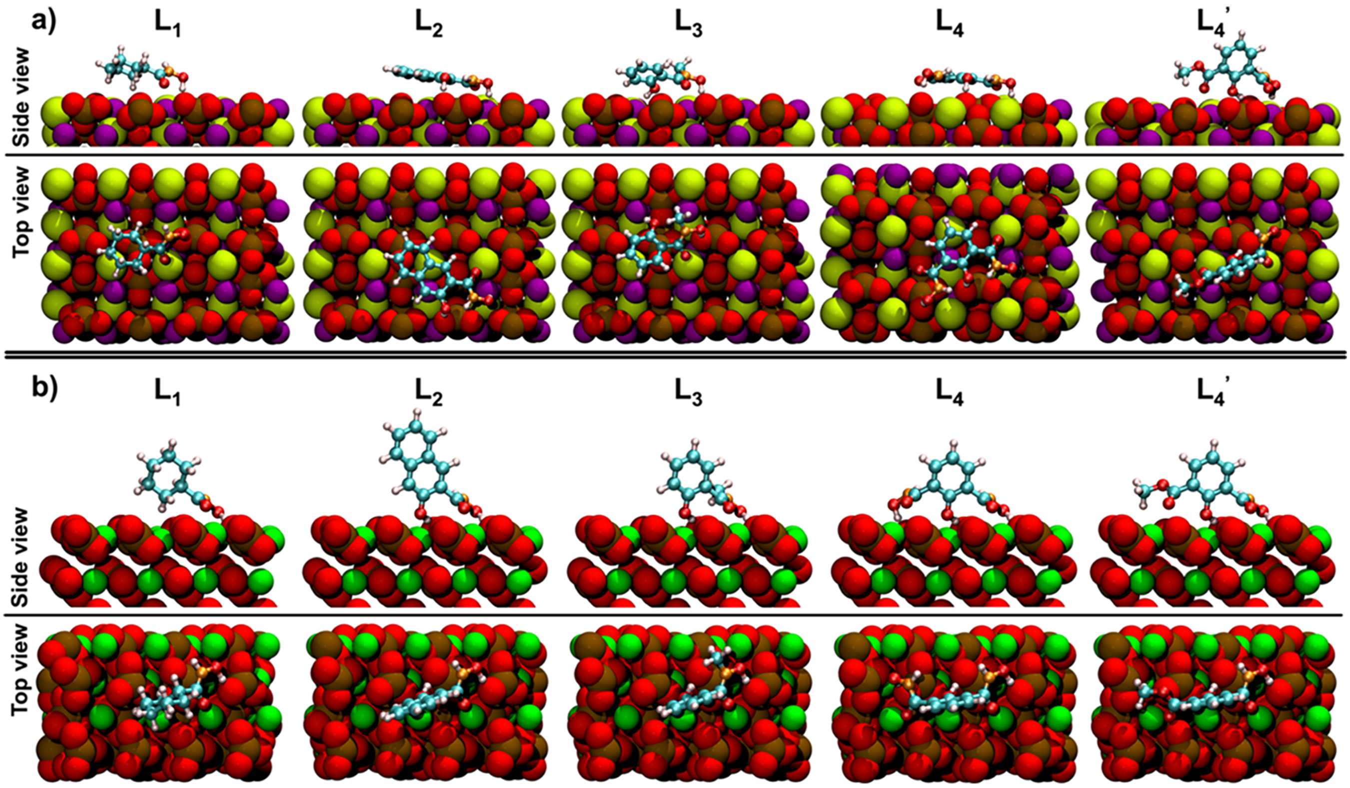

Figure 3. Minimum-energy structures of L$_1$ through L$_4$ and L$_4$′ adsorbed onto (a) bastnäsite-[10$\bar{1}$0] and (b) calcite-[10$\bar{1}$4] at low coverage. Side-view images have been truncated below the second layer. Color scheme: Ce: lime, F: purple, Ca: green, C: cyan/brown, O: red, N: orange, and H: white.

system was split into two paths: one directed to a pulse shaper to generate narrow band near infrared pulses with about 1 nm bandwidth centered near 800 nm. The second arm was sent to an optical parametric amplifier and difference frequency mixer to generate mid-infrared (IR) pulses centered at ~2900 cm^{-1}. These two arms were colinearly combined using a dichroic mirror and focused on the bastnäsite sample at a ~60° angle with respect to the surface normal. The radiated light was polarization resolved and spectrally dispersed using a CCD camera for detection. Isotherms were obtained by depositing ligand solutions (prepared at pH ~ 8.5) onto the surface and allowing them to incubate for several minutes before wicking away excess liquid. Our previous work[42] has shown residual water at the interface during measurements, but not enough to attenuate the incident light or steer the beams due to refraction. Orientational measurements were made by varying the polarization combinations probed by vSFG and following the procedure described elsewhere.[67,68] The SSP and PPP combinations were probed, the letters describe in order the polarizations of light in decreasing energy, that is, SSP, S-polarized vSFG, S-polarized NIR, and P-polarized IR fields. The bastnäsite samples were prepared as described previously.[42] They were cleaned after experiments with methanol and stored in copious amounts of water overnight in between experiments. In all cases, the vSFG signals were scaled by the nonresonant response of the cleaned bastnäsite sample in the absence of the ligand.

Infrared Spectroscopy. ATR-FTIR spectra were recorded using a 45° single-reflection diamond/ZnSe internal reflection element (PIKE Technologies GladiATR). To characterize the spectral features of each ligand in solution and bonded to cerium, aqueous phase spectra were compared with and without the addition of cerium. Solutions were prepared at concentrations near saturation for each ligand (5−10 mM) and then adjusted to pH 9 using NaOH. Spectra were recorded against a background of pH 9 water (NaOH). CeCl$_3$ (0.1 M) was then added until the ligand solution became colored and cloudy, and spectra were recorded. Due to the limited solubility of the ligands, FTIR bands were very weak in the presence of water. Upon the addition of CeCl$_3$, peaks not only shifted in position but also increased in intensity as a precipitate began to form and settle on the reflection element.

To measure the spectra of adsorbed ligands in situ, a thin film of bastnäsite particles was formed by allowing a suspension of synthetic bastnäsite in methanol to dry on the internal reflection element. The film was rinsed with DI water before measuring a background of the film under ~2 mL of water. The water was then removed with a pipette and replaced with the ligand solution. The concentration used for adsorption was 0.5 mM for each ligand, except for L$_4$′, which features one hydroxamate and one ester functional group and was measured at 0.25 mM. Spectra of the film in ligand solution were taken after 1, 5, and 10 min intervals over the course of 1 h. The ligand solution was removed with a pipette and replaced with a fresh solution between each measurement.

Raman Spectroscopy. Raman spectra were recorded using a XploRA spectrometer (Horiba) coupled with an Olympus microscope equipped with a 10× (0.25 NA) objective. The spectrometer was set to use a 300 μm pinhole and a 600 or 1800 line/mm grating. Spectra were recorded using a 638 nm laser. The solutions of ligands were prepared with a final concentration of 0.1 mM at pH ~8.5−9. Raman spectra of these solutions were acquired by placing a drop of the solution on the bastnäsite crystal after which, spectra were recorded after ~30 min. Pure ligands were measured in a powder form.

X-ray Photoelectron Spectroscopy. XPS was performed using a Thermo Scientific (Waltham, MA, USA) Model K-Alpha XPS instrument. The instrument utilized monochromated, micro-focused, Al K$_\alpha$ X-rays (1486.6 eV) with a variable spot size (i.e., 30−400 μm). Analyses of the sample were performed with a 400 μm X-ray spot size that yielded maximum signal with an effort to obtain signal over the largest possible area. Emitted photoelectrons were resolved using a hemispherical electron energy analyzer equipped with a 128-channel detector system. The sample was mounted on a metal base that, in turn, was clipped to the K-Alpha sample holder. The sample was

Table 1. Adsorption Energies (kJ/mol) of Minimum-Energy Structures of L_1 through L_4 and L_4' at Low Coverage on the Bastnäsite-[$10\bar{1}0$] and Calcite-[$10\bar{1}4$] Surfaces, Calculated Using eqs 1 and 2

surface	SHA	BHA	L_1	L_2	L_3	L_4	L_4'
bastnäsite-[$10\bar{1}0$]	−48.9[a]	−50.1[a]	−51.9	−57.5	−61.8	−54.8	−44.5
calcite-[$10\bar{1}4$]	−59.2[a]	−42.0[a]	−40.7	−62.5	−75.3	−55.2	−24.1
bastnäsite-[$10\bar{1}0$] + $16H_2O$	−75.2	−65.3			−66.3	−97.5	
calcite-[$10\bar{1}4$] + $16H_2O$	−68.9	−47.4			−63.3	−66.6	

[a] Adsorption energies from ref 42. The corrected adsorption energy for BHA on calcite-[$10\bar{1}4$] is given.

analyzed after polishing/rinsing and after exposure to the ligand-containing solution. After transferring the sample into the analysis chamber, a survey spectrum (pass energy = 200 eV) was acquired to identify all elements present at the sample surface. Next, high-resolution core level spectra (pass energy = 50 eV) were recorded for detailed chemical state analysis. All spectra were recorded with a charge neutralization flood gun (combination of low energy electrons and argon ions) to maintain a stable analysis condition. The typical pressure in the analysis chamber with the flood gun operating is 2 × 10^{-7} mbar. Data were collected and processed using the Thermo Scientific Avantage XPS software package (v.5.96). The survey XPS spectra of bastnäsite, L_4'-treated bastnäsite, and pure L_4' are presented in the Supporting Information. The L_4'-treated bastnäsite was prepared by placing bastnäsite into aqueous solution with the concentration of ligand 0.1 mM and pH 8.5 for an hour, followed by excessive washing with water and subsequent drying of the crystal.

■ RESULTS AND DISCUSSION

DFT Studies of Monolayer Ligand Absorption in the Absence of Explicit Water Solvent. The minimum-energy structures of adsorbed L_1 through L_4 and L_4' on the bastnäsite-[$10\bar{1}0$] surface are presented in Figure 3a, and adsorption energies in Table 1. Previously, we reported adsorption structures and energies for SHA on this surface using the same DFT treatment described in the Methods section.[39] Herein, for ligand L_1 through L_4, we find a single metal−ligand interaction between the carbonyl oxygen atom in the hydroxamic acid moiety and a Ce atom on the bastnäsite surface [$d(=\!O{-}Ce) = 2.43$ Å]. For SHA we also find two hydrogen bonds that arise from the hydroxyl hydrogen atoms in both the phenolic [$d(H{-}O_{surface}) = 1.57$ Å] and the hydroxamic acid (1.64 Å) groups to the carbonate oxygen atoms at the surface, with the aromatic ring lying flat on the surface. Similarly, L_1 through L_4 also show surface-parallel ligand ring orientations and similar interactions with the surface atoms. All four surface-parallel ligands show exactly one interaction with a surface Ce ion, via the carbonyl oxygen atom, with similar interatomic distances, consistent with the adsorption mechanism of the alkyl hydroxamic acid[18] at low surface coverages (Table S1). Notably, though hydroxamic acid moieties have been shown to be responsible for strong ligand adsorption via interactions with metal atoms on the mineral surface,[42] L_4, with two hydroxamic acid groups, exhibits only a single metal−ligand interaction. We attribute this to the poor alignment of the structure of the ligand which, in the absence of any surface, shows O−O distances between both hydroxamic acid groups of 6.4−6.5 and 8.5−8.8 Å (Figure S1 and Table S3), with the arrangement of metal ions on the surface, which shows distances between surface Ce ions of 7.1 Å along the long axis and 4.8 Å along the short axis. In contrast to L_1 through L_4 adsorption, L_4' exhibits a surface-perpendicular structure. Additionally, L_4' interacts with two surface metal atoms through both carbonyl oxygen atoms [$d(Ce{-}O_{hydroxamic\ acid\ carbonyl}) = 2.48$ Å and $d(Ce{-}O_{ester\ carbonyl}) = 2.52$ Å] and the phenolic hydroxyl oxygen [$d(Ce{-}O_{phenol}) = 2.75$ Å]. The ester carbonyl oxygen and phenolic hydroxyl oxygen interact with the same surface metal atom in a bidentate fashion, whereas the hydroxamic acid carbonyl oxygen interacts with the next closest surface metal atom.

As a general feature, we find that all hydroxamic-acid hydroxyl groups donate a hydrogen bond to an electronegative atom on the bastnäsite surface: L_1 and L_3 interact with a surface oxygen atom on carbonate [$d(H{-}O_{surface}) = 1.61$ Å and 1.62 Å, respectively], whereas L_2 interacts with a surface fluorine [$d(H{-}F_{surface}) = 1.64$ Å]. With two hydroxamic acid groups, L_4 donates hydrogen bonds to both an oxygen [$d(H{-}O_{surface}) = 1.81$ Å) and a fluorine $d(H{-}F_{surface}) = 1.64$ Å] on the surface. On L_4', the hydroxyl hydrogen in the hydroxamic acid group interacts with both a surface fluorine [$d(H{-}F_{surface}) = 2.37$ Å] and surface carbonate oxygen [$d(H{-}O_{surface}) = 2.36$ Å]. Ligands containing phenolic groups also donate hydrogen bonds to electronegative surface atoms: L_2, L_4, and L_4' to surface oxygen atoms [$d(H{-}O_{surface}) = 1.58$, 1.48, and 1.44 Å, respectively], and L_3 to a surface fluorine [$d(H{-}F_{surface}) = 1.73$ Å].

Notably, the adsorption energies (eq 1) for L_1 through L_4, L_4', and SHA show a disparity in the total number of ligand−surface interactions contributing to adsorption. L_1, for example, shows stronger adsorption ($E_{ads} = -51.9$ kJ/mol) than SHA ($E_{ads} = -48.9$ kJ/mol[42]) despite lacking the phenolic moiety and associated hydrogen bonds that can form with the surface to further stabilize the complex. Moreover, L_2, which differs from SHA only by the relative extension of the phenolic group to a naphtholic moiety, shows a similar orientation with respect to the surface and nearly identical interactions contributing to adsorption as SHA. In fact, characteristic ligand−surface interaction distances differ by ≤0.01 Å each for SHA and L_2 on bastnäsite-[$10\bar{1}0$]. Despite this, L_2 shows stronger adsorption onto the surface ($E_{ads} = -57.5$ kJ/mol) than SHA, stronger than we would expect merely due to increased van der Waals interactions with the surface inherent to the extension of the aromatic moiety. To elucidate the chemical nature of these apparent inconsistencies, we probed the effect of modifying the van der Waals damping function parameter (vdW_S_8) within Grimme's D3 dispersion correction expression.[53] Previous theoretical work examining surface interactions of inorganic minerals[69] showed better agreement with experimental exfoliation energies (i.e., mineral layer adsorption) when the vdW_S_8 parameter is scaled by a factor of 0.27. Indeed, when we decreased the S_8 value from the default value of 0.772 to 0.208, we found that the difference in adsorption energies of optimized SHA and L_2 on the bastnäsite surface decreased from 8.56 kJ/mol to a more reasonable 3.95 kJ/mol. Thus, we suspect that the D3 correction, as applied with default settings, likely leads to hydrocarbon moieties overbinding onto the bastnäsite-[$10\bar{1}0$] surface. Future work shall explore this overestimation further and consider an alternative treatment, for example, with the van der Waals density functional (vdW-DF) family of non-local correlation-functionals.[70] In the meantime, care must be taken when implementing a D3 dispersion treatment on adsorption complexes of minerals with ligands containing extended aliphatic or aromatic regions. The use of an implicit solvent in the absence of explicit solvent can also lead to inaccuracies in the predicted adsorption energies, as described below.

Additionally, L_4' exhibits slightly weaker adsorption (E_{ads} = −44.5 kJ/mol) than SHA despite the inclusion of an additional surface metal interaction by the ester group. L_4' adsorption on bastnäsite-$[10\bar{1}0]$ is also less stable than L_4 by 10 kJ/mol. This effect is likely due to the weak interaction between the ester carbonyl and the surface metal atom, which displays a longer bond length than hydroxamic acid carbonyl interactions. Surface-parallel structures of L_4' adsorption are not favored because the O−O distance does not align well with surface metal atoms and it cannot donate a hydrogen bond to the surface to overcome the poor alignment as with the L_4 ligand. Although L_4 can also adopt a similar perpendicular adsorption structure with a very similar adsorption energy (44.0 kJ/mol), it is still more energetically favorable (by 10.8 kJ/mol) for L_4 to lie flat along the bastnäsite-$[10\bar{1}0]$ surface.

Differences in metal ion spacing lead to different adsorption modes on the calcite-$[10\bar{1}4]$ surface as compared to the bastnäsite-$[10\bar{1}0]$. Neighboring Ca−Ca distances are shorter (i.e., 4.0 Å along the long axis and 5.0 Å along the short axis) than analogous Ce−Ce distances in bastnäsite. As a result, to adsorb onto calcite-$[10\bar{1}4]$ most effectively, ligands must rotate out of a planar orientation to be perpendicular to the surface plane, as shown in Figure 3b. However, as on the bastnäsite-$[10\bar{1}0]$ surface, the ligands on the calcite-$[10\bar{1}4]$ surface show similar adsorption modes to those of SHA. The oxygen atoms in all ligands interact with surface Ca sites, showing similar $Ca-O_{carbonyl}$ distances (2.34−2.36 Å for all ligands, 2.62 Å for the additional hydroxamic group in L_4, and 2.77 Å for the ester group in L_4'), $Ca-O_{hydroxamic\ acid\ hydroxyl}$ (2.53−2.75 and 3.53 Å, respectively), and $Ca-O_{phenol}$ (2.43−2.48 Å) distances, where applicable, across the series of adsorbates. Furthermore, all hydroxyl hydrogen atoms interact with surface oxygen atoms across all ligands, namely, $(O)H_{hydroxamic}-O_{surface}$ (1.38−1.40 Å for all five ligands, and 1.54 Å for the additional hydroxamic group in L_4) and $H_{phenol}-O_{surface}$ (1.39−1.49 Å). These distances are detailed in Table S2.

Adsorption onto the calcite-$[10\bar{1}4]$ surface is stronger than on bastnäsite-$[10\bar{1}0]$ in the cases of SHA, L_2, and L_3, whereas BHA, L_1, and L_4' exhibit weaker adsorption. L_4 is the only ligand that displays effectively no change in adsorption strength between bastnäsite and calcite surfaces (E_{ads} = −54.8 and −55.2 kJ/mol, respectively). Of the ligands of interest in this study, only L_2 and L_3 exhibit stronger adsorption (E_{ads} = −62.5 and −75.3 kJ/mol, respectively) than SHA on calcite, which deviates from the trend that is seen on bastnäsite where every ligand but L_4' demonstrated stronger adsorption than SHA.

The only difference between BHA and L_1 is the loss of aromaticity in the ring structure where the ring on L_1 is fully hydrogenated. Given that both ligands adsorb with a structure that is not surface-parallel, the similarity in their adsorption energies is not surprising (E_{ads} = −42.0 and −40.7 kJ/mol, respectively). The same rationale can also justify the similar adsorption energies between SHA and L_2 (E_{ads} = −59.2 and −62.5 kJ/mol, respectively), where L_2 substitutes the phenyl moiety in SHA for a naphthyl moiety.

L_3 exhibits stronger adsorption than SHA on calcite-$[10\bar{1}4]$, which matches the trend seen on bastnäsite. However, this phenomenon of improved adsorption via inclusion of a methyl group is confounding because there are no obvious interactions between the methyl group and surface atoms. A possible explanation for this phenomenon can again be attributed to the treatment of dispersion corrections, which show that the D3 correction for L_3 on calcite is 14.5 kJ/mol more stabilizing than SHA on calcite. This peculiar behavior is addressed in a later section wherein explicit water molecules are included in the calculations.

The nearly unchanged adsorption energy for L_4 on calcite versus bastnäsite implies that the loss of favorable dispersion interactions with the bastnäsite surface is almost exactly counterbalanced by the interaction of the second hydroxamic acid group with a surface metal atom on calcite. The perpendicular orientation of L_4 on calcite also allows for a greater interaction between the exposed surface atoms and the implicit water solvent (compared to the surface-parallel orientation of L_4 on bastnäsite). Despite the extra surface metal interaction, L_4 still exhibits a lower adsorption energy than SHA on calcite-$[10\bar{1}4]$. This result is likely due to the loss of two intramolecular hydrogen bonds that are present in the most stable conformation of L_4 in solution (i.e., they are absent when adsorbed to the surface), whereas SHA only loses a single intramolecular hydrogen bond during adsorption.

L_4' closely mimics the adsorption structure of L_4 but displays the lowest adsorption energy on calcite-$[10\bar{1}4]$ among all ligands of interest (E_{ads} = −24.1 kJ/mol), which is attributed to potentially subtle molecular details. First, L_4' must sacrifice two intramolecular hydrogen bonds to enable ligand−surface interactions, which negatively impacts adsorption energetics. Second, the ester group interacts with surface atoms weaker than the secondary hydroxamic acid group in L_4, which is demonstrated by the longer $Ca-O_{ester\ carbonyl}$ bond distance [$d(=O_{ester}-Ca)$ = 2.77 Å versus $d(=O_{hydroxamic}-Ca)$ = 2.62 Å] and the lack of a hydrogen bond donor. Lastly, due to the most stable s-cis or Z conformation of the ester (in which the dihedral angle C−O−C=O is close to zero), the methyl group obscures the interaction of surface carbonate oxygen atoms with the implicit water solvent, further diminishing the adsorption energy on calcite-$[10\bar{1}4]$.

DFT Studies of Monolayer Ligand Absorption in the Presence of Two Monolayers of Water. The implicit treatment of solvent—that is, by means of a correction to electronic energy based on the dielectric constant of water—provides insights into the interaction between bulk solvent and adsorbed ligands as contributing, for example, to a difference in the adsorption energies of ligands on the calcite-$[10\bar{1}4]$ surface due to variations in the presentation of hydrophobic moieties into the implicit solution medium. However, the treatment of solvent in this manner neglects specific interactions among individual solvent molecules, adsorbed ligands, and the surface, which may be integral to adsorption and, more importantly, may further differentiate descriptions of adsorption across a series of ligands. Thus, to improve our understanding of ligand adsorption onto mineral surfaces in froth flotation slurries, we have begun to explicitly add water molecules at the adsorbate—mineral interfaces. As elaborated in the Methods section, beginning with the most stable hydroxamic acid ligand−surface structures in the absence of explicit water, we

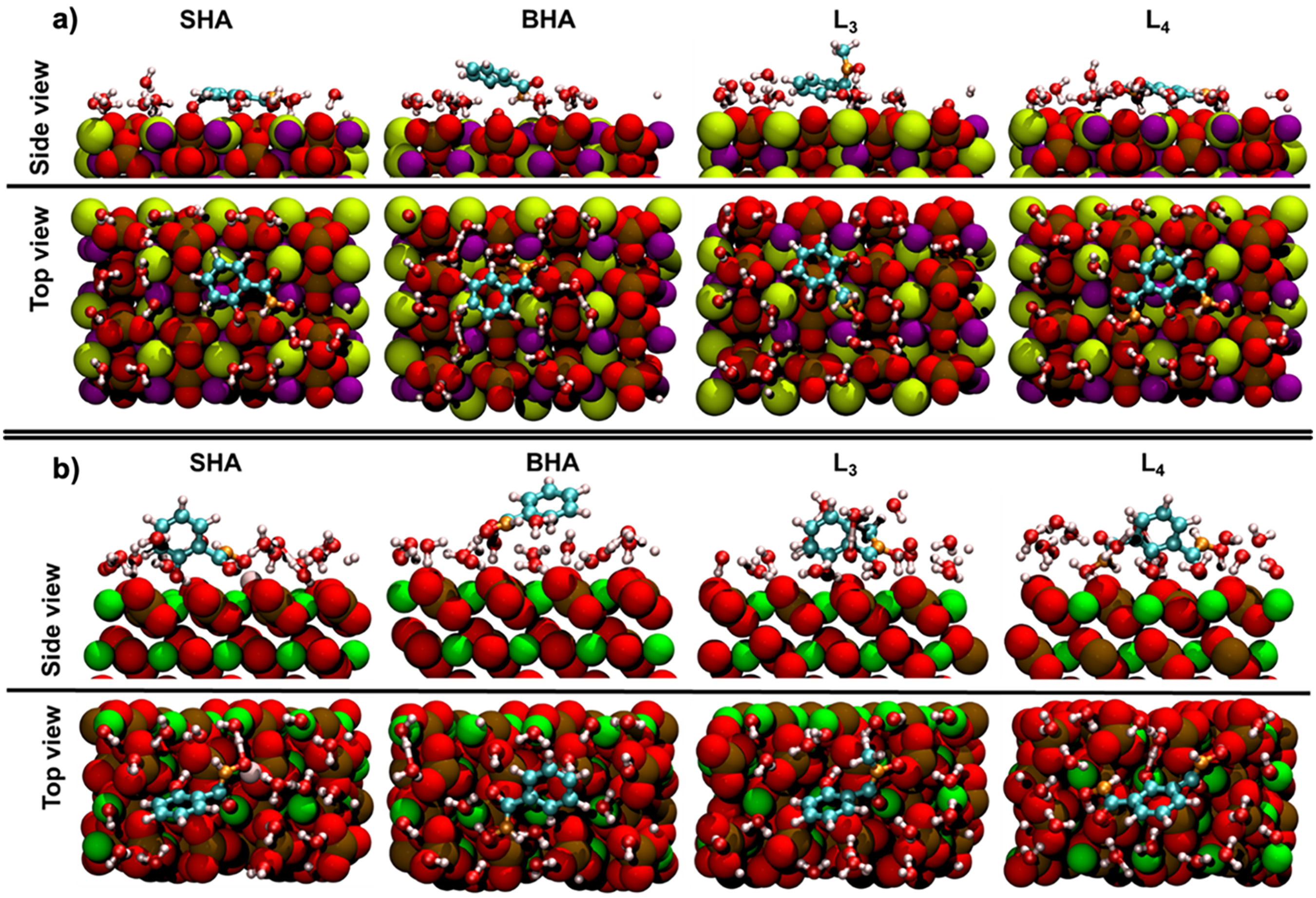

Figure 4. Minimum-energy structures of SHA, BHA, L_3, and L_4 adsorbed onto (a) bastnäsite-[$10\bar{1}0$] and (b) calcite-[$10\bar{1}4$] at low ligand coverage in the presence of two explicit water molecules per surface cation. Side-view images have been truncated below the second layer. Same color scheme as in Figure 3.

have added two water molecules for each surface metal cation for a total of 16 water molecules for each adsorbed hydroxamic acid ligand. Configurational sampling in the presence of 16 water molecules due to high computational cost was limited to BHA, SHA, and new ligands L_3 and L_4. Previously reported ligands L_1 and L_2,[43,44] showed difficulties related to the treatment of dispersion forces in systems without explicit water (vide supra), were not subject to explicit solvation. L_4' was also excluded from the explicit solvation calculations because it exhibited the weakest adsorption energies among all the ligands for both bastnäsite-[$10\bar{1}0$] and calcite-[$10\bar{1}4$] surfaces. Figure 4a shows lowest-energy structures resulting from AIMD simulations and subsequent geometry optimizations of explicitly solvated SHA, BHA, L_3, and L_4 on bastnäsite-[$10\bar{1}0$].

SHA, in the presence of explicit water, shows similar interactions with the surface as was found with implicit solvation models. The hydroxamic acid moiety contributes to adsorption via an interaction between the carbonyl oxygen and a Ce ion [d(=O−Ce) = 2.48 Å] and the hydrogen-bond donation from the hydroxyl hydrogen is now directed to a surface fluorine {d[(O)H−F] = 1.52 Å}. Similarly, the phenolic group donates a hydrogen bond to a surface oxygen [$d(\mathrm{H_{phenol}{-}O_{surface}})$ = 1.54 Å]. In addition to these interactions, a single water molecule donates a hydrogen bond to the hydroxamic acid hydroxyl group {$d[\mathrm{(N)O{-}H_{water}}]$ = 1.76 Å}. As a result of these interactions, SHA shows an orientation with respect to the surface that is nearly parallel and an adsorption energy of −75.2 kJ/mol. Furthermore, the intramolecular hydrogen bond is maintained {$d[\mathrm{(N)H{-}O_{phenol}}]$ = 1.77 Å}.

The *N*-methyl-substituted L_3 also adsorbs via a carbonyl−Ce interaction (d = 2.46 Å) and hydrogen-bond donation from the phenol [$d(\mathrm{H_{phenol}{-}O_{surface}})$ = 1.55 Å]. However, the hydroxamic acid hydroxyl group now donates its hydrogen bond to a solvent molecule [$d\mathrm{(O)H{-}O_{water}}$ = 1.71 Å] instead of to a surface moiety. The accepting water molecule, in turn, interacts with a surface fluorine. Additionally, the ligand accepts hydrogen bonds from two neighboring water molecules, at the carbonyl oxygen [$d(\mathrm{{=}O{-}H_{water}})$ = 2.50 Å] and phenolic oxygen [$d(\mathrm{O_{phenol}{-}H_{water}})$ = 1.71 Å] atoms. As a result of the disruption of a ligand−surface interaction by a water molecule in the hydroxamic acid moiety, L_3 adsorbs weaker than SHA onto bastnäsite-[$10\bar{1}0$] in the presence of explicit water (E_{ads} = −66.3 kJ/mol). While the lack of an intramolecular hydrogen bond in L_3, imparting additional flexibility, enhances adsorption relative to SHA in the absence of explicit solvent, this same flexibility allows for an explicitly included water molecule to compete for surface sites and limit ligand adsorption by hindering direct ligand−metal interactions. The rigidity of SHA, due to its intramolecular hydrogen bond, prevents a water molecule from adsorbing between the ligand and the surface, thereby facilitating stronger ligand−bastnäsite interactions and contributing to stronger adsorption.

Interestingly, benzohydroxamic acid (BHA, Figures 1 and 4), which lacks a phenolic group, thereby precluding an intramolecular hydrogen bond, does not adsorb via a direct interaction with a surface Ce in the presence of explicit solvent. A single ligand−surface hydrogen bond, donated by the hydroxamic-acid hydroxyl group, as well as four hydrogen bonds with explicit solvent water molecules, contribute to adsorption, with a similar adsorption energy (E_{ads} = −65.3 kJ/mol) as L_3. As in the case of L_3, the flexibility of BHA allows for water molecules to remain between the ligand and the surface upon adsorption. The strength of BHA adsorption, despite the lack of a direct metal—BHA interaction, suggests that the hydroxamic acid group interacts favorably with the hydrogen bond network present on the bastnäsite-$[10\bar{1}0]$ surface while still maintaining a close to surface-parallel orientation, thereby enabling adsorption without extensive direct interaction.

L_4, similar to SHA, shows a ligand−surface interaction between the carbonyl oxygen and a surface Ce site (d = 2.47 Å) and hydrogen-bond donation to a surface fluorine {d[(O)H−F] = 1.62 Å} from one of the hydroxamic acid moieties, as well as hydrogen-bond donation from the phenol group to a surface oxygen atom [$d(H_{phenol}-O_{surface}$ = 1.43 Å]. Both oxygen atoms in the additional hydroxamic acid moiety accept hydrogen bonds from solvent molecules {$d(=O-H_{water})$ = 1.70 Å, $d[(H)O-H_{water}]$ = 2.04 Å}. L_4 maintains both intramolecular hydrogen bonds, which enhance adsorption, as with SHA. It is the greater extent of interaction with water molecules; however, that contributes to stronger adsorption in L_4 (E_{ads} = −97.5 kJ/mol).

Once again without mitigation from intramolecular hydrogen bonding, as shown in Figure 4b, SHA and L_3 show similar direct interactions with the calcite-$[10\bar{1}4]$ surface {$d(=O-Ca)$ = 2.40 Å for both systems; $d[(O)H_{hydroxamic\ acid}-O_{surface}]$ = 1.45 Å for SHA and 1.61 Å for L_3; and $d(H_{phenol}-O_{surface})$ = 1.50 Å for SHA and 1.62 Å for L_3}. Interactions between each of the two ligands and solvent molecules differ due to substitution on the nitrogen atom, however contributing to differences in adsorption on the explicitly solvated calcite-$[10\bar{1}4]$ surface. SHA, with a hydrogen atom bound to this nitrogen, participates in hydrogen-bonding interactions with three water molecules; the amino hydrogen atom interacts with one solvent molecule (d = 1.85 Å), and the hydroxamic-acid hydroxyl oxygen atom with two solvent molecules (d = 1.50 and 1.73 Å). Meanwhile, the methyl substituent in L_3 precludes hydrogen bonding around the nitrogen atom and prevents solvent water molecules from approaching the hydroxamic-acid hydroxyl group via steric repulsion, such that only one explicit interaction with solvent at the carbonyl oxygen [$d(=O-H_{water}$] is present. Thus, all three ligand−solvent interactions found in calcite-$[10\bar{1}4]$ bound SHA are absent in the L_3-adsorbed system, weakening adsorption of the latter ligand (E_{ads,L_3} = −63.3 kJ/mol). However, in the absence of explicit water, discussed above, SHA displayed weaker adsorption than L_3, which highlights the importance of explicit water interactions when evaluating ligand adsorption on mineral surfaces.

L_4, as expected, shows a greater extent of adsorption interactions with the surface than SHA due to its additional hydroxamic acid substituent. As such, both hydroxamic acid moieties interact with surface Ca ions, albeit through different modes. As in SHA, one hydroxamic acid group shows interaction via the carbonyl oxygen (d = 2.32 Å), but the other interacts via the hydroxyl oxygen (d = 2.55 Å). The phenolic group also interacts with a surface cation [$d(O_{phenol}-Ca)$ = 2.44 Å]. Beyond metal−ligand interactions, differences contributing to SHA and L_4 adsorption persist. Both hydroxamic acid hydroxyl groups in L_4 donate hydrogen bonds to surface oxygen atoms {$d[(O)H-O_{surface}]$ = 1.51 and 1.74 Å}, similar to SHA. However, the phenolic group in L_4 donates its hydrogen atom to a solvent molecule, which continues to interact with its donor [$d(O_{phenolate}-H_{hydronium})$ = 1.43 Å]. This serves as a promising example of the capabilities afforded by extended explicit solvation in predicting the protonation state of an adsorbed ligand in solution. Although the second hydroxamic acid group on L_4 interacts with a surface Ca atom, it does so through the hydroxyl oxygen, which provides a weaker interaction than the carbonyl oxygen. The non-adsorbing carbonyl moiety interacts with two water molecules {$d[=O-H_{water}]$ = 1.64 and 1.95 Å}, but the overall interaction of the second hydroxamic acid group with the surface is still less favorable than the explicit solvation of the corresponding surface atoms. This is demonstrated by the stronger adsorption of SHA (E_{ads} = −75.2 kJ/mol) versus L_4 (E_{ads} = −66.6 kJ/mol) on calcite-$[10\bar{1}4]$.

Attenuated Total Reflectance Fourier Transform Infrared Studies. In our previous work,[42] we presented attenuated total reflectance Fourier transform infrared (ATR-FTIR) spectra of SHA adsorbed onto bastnäsite at pH 8.5, as relevant to a practical flotation environment. In the present work, we use FTIR spectra as a basis for comparison with those of ligands L_1 through L_4'—functionalized derivatives of SHA—on the same mineral surface in order to provide experimental insights into the adsorption of these new ligands. When referring to an intense C=O stretch band around 1600 cm^{-1} for a free ligand, we note that these modes are strongly coupled to the other modes, such as the aromatic C−C stretches. However, for aromatic ligands that are chelated to Ce^{3+}, DFT calculations show that the vibrational amplitude arises from the vibrations of the aromatic C−C bonds at ~1600 cm^{-1}, but we retain the same notations for simplicity. As in the adsorbed-SHA spectra,[42] we expect that the frequencies of several vibrational modes will overlap with one another, and significantly with intense vibrations of the underlying bastnäsite solid (~1350−1525 cm^{-1}) and the water bending mode (~1640 cm^{-1}), making a detailed assignment of frequencies difficult. However, several prominent spectral bands lend themselves to meaningful analysis.

Outside the range of frequencies dominated by the bastnäsite solid, the ATR-FTIR spectra of L_1 on bastnäsite (Figure S3) exhibits a pronounced feature around 1600 cm^{-1}. This C=O stretching vibration is also seen for solution-phase L_1 when complexed with a cerium(III) ion. However, in contrast to SHA, very few spectral features are present beyond the C=O stretching band due to the lack of any aromatic rings or additional functional groups in the L_1 molecule. The adsorption mechanism is likely to be the same to that of alkyl hydroxamate on bastnäsite,[19] which was interpreted as bidentate complexation of the hydroxamate functional group at high ligand concentration (1 mM).

The spectrum of L_2 on bastnäsite (Figure S4) shows significant bands similar to adsorbed SHA,[42] including C=O stretching modes at ~1600 cm^{-1} and phenolic C−O bands at about 1225 and 1265 cm^{-1}. However, due to the extended aromatic moiety in L_2 as compared to that of SHA, four modes

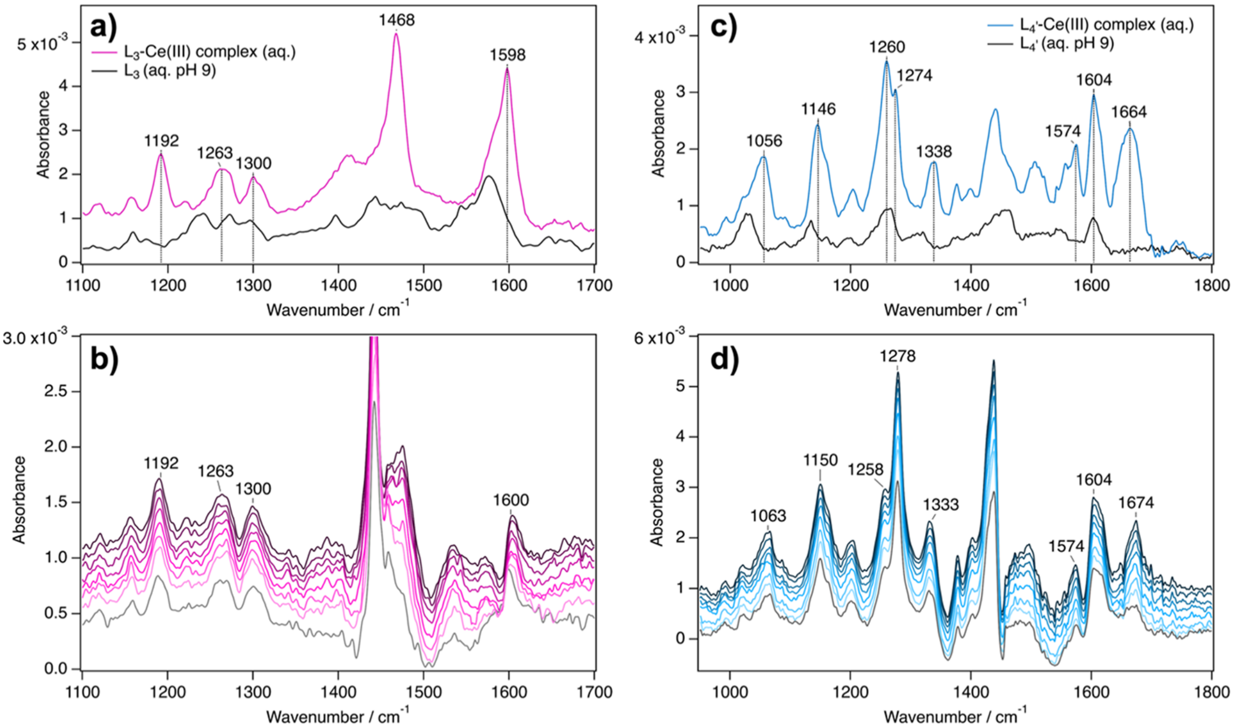

Figure 5. ATR-FTIR spectra for L_3 (a) and L_4' (c) in aqueous solution (black traces) and with aqueous Ce^{3+} in solution (purple traces), and time-resolved adsorption of L_3 (b) and L_4' (d) onto bastnäsite over 1 h (light to dark).

including C−C vibrations of the aromatic rings with C−N and N−O contributions, are seen in the 1030−1200 cm^{-1} region of the L_2−bastnäsite spectrum, as opposed to two for SHA—bastnäsite. The similarity of ATR-FTIR spectra for these two systems agrees with DFT results revealing nearly identical binding modes for L_2 and SHA on the bastnäsite-[$10\bar{1}0$] surface (Figure 3a). All bands remained after rinsing the film with DI water, indicating strong adsorption of L_2 on the mineral surface.

The spectra of L_3, shown in panels a and b of Figure 5, also reveal similarities with those of SHA on bastnäsite. Following the exposure of the mineral surface to L_3 (Figure 5a), a C═O stretching mode at ∼1600 cm^{-1} is present, as are two phenolic C−O features at 1263 and 1300 cm^{-1}. However, the peak at 1151 cm^{-1} in the adsorbed SHA spectrum—a combination band with contributions for C−N, N−O and aromatic C−C stretching and C−C bending—has been shifted to ∼1192 cm^{-1} in the bastnäsite−L_3 spectrum, as a result of the methyl substitution on the hydroxamic acid nitrogen. In further contrast to the spectrum of the SHA system, the ATR-FTIR intensities are noticeably weaker, perhaps indicating weaker adsorption, once again supporting DFT adsorption energies uniquely on the defect-free surface in the presence of explicit water. Overall, the positions of the peaks and the corresponding band shifts induced by the presence of Ce^{3+} ions are well reproduced by the DFT calculations assuming a bidentate coordination of the deprotonated ligand. In particular, computational results show a notable shift in the C═O stretch band to a higher frequency (by 18 cm^{-1}) upon bidentate coordination, a trend consistent with experimental results (Figure 5).

In contrast to SHA, the ATR-FTIR spectra of L_4', both in aqueous complexes with Ce^{3+} ions and on the surface of bastnäsite, show a significant splitting of the C═O stretching frequency relative to that of a free deprotonated ligand in solution. This vibrational mode, at 1604 cm^{-1} in the absence of any metal ion or mineral surface (Figure 5, panel d, black trace), splits into two features in aqueous complexes (at 1574 and 1664 cm^{-1}) and similarly on the bastnäsite surface. This splitting is consistent with bidentate chelation, as seen for salicylic acid on the bastnäsite surface.[42] This is further supported by DFT calculations showing a small separation between the two intense C═O vibrational modes coupled with the aromatic C−C vibrations (1591 and 1620 cm^{-1}) in the deprotonated form of L_4' and a much larger separation when the ligand is chelated to Ce^{3+} (1578, 1599, and 1656 cm^{-1}). The feature at 1604 in the L_4'−bastnäsite spectrum is broader than that seen in either the aqueous L_4'−Ce^{3+} complex or on the SHA−bastnäsite complex, perhaps suggesting multiple types of uncoordinated and coordinated hydroxamic and ester moieties, including those in bulk as well as those on the surface which directly interact with surface cations. The latter is exemplified in our DFT results for L_4' (Figure 3a). A broad C−O stretching mode of the phenolic moiety coupled with C−C vibrations at around 1260 cm^{-1} in the solution-phase spectrum of L_4' is split into multiple features when L_4' is complexed in solution (at 1260 and 1274 cm^{-1}) or adsorbed on the bastnäsite surface (at 1258 and 1278 cm^{-1}). This splitting, not otherwise seen for ligands L_2 and L_3 with a single hydroxamic acid moiety, suggests that the phenolic C−O stretching mode has contributions from vibrations of the hydroxamic moiety and the ester moiety in L_4'. The relative intensities of these two features varies depending on the REE-containing environment. In the aqueous-Ce^{3+} system, the peak intensities of both bands are similar, and the separation between bands is small (14 cm^{-1}). For the bastnäsite system, the higher-wavenumber feature is much more intense than the lower-wavenumber feature, and the separation between bands (20 cm^{-1}) is greater than in the solution-phase Ce^{3+} system. The peak for deprotonated L_4' in the absence of any metal at

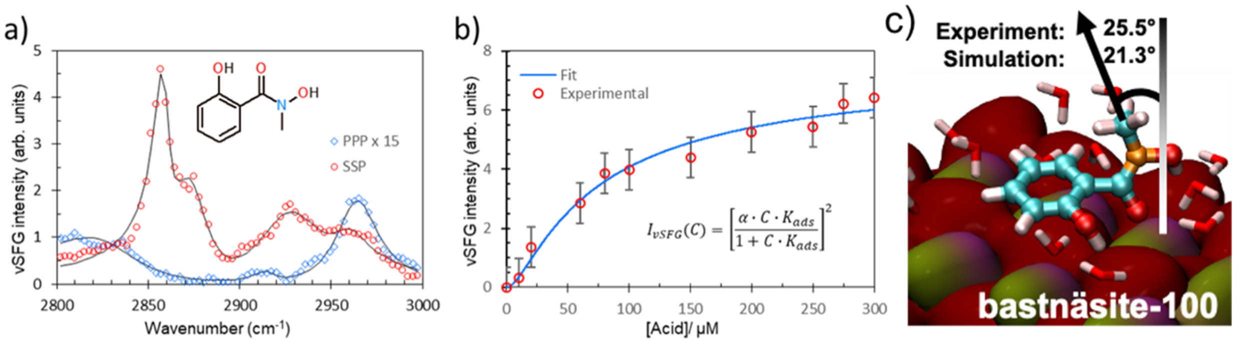

Figure 6. vSFG results for L_3 on bastnäsite-[$10\bar{1}0$]. (a): Spectra from PPP (blue) and SSP (red) polarizations. (b) vSFG intensity with respect to L_3 concentration. Data points (red) show a standard deviation around the mean, and the blue trace shows the fit of the Langmuir isotherm in eq 3 to the data. (c) Illustration of the orientation angle obtained from vSFG spectra. Color scheme for atoms in (c): C: gray, O: red, N: blue, and H: white.

1133 cm^{-1} is assigned to the ester C−O stretch coupled to several in-plane vibrations. It is shifted to higher frequencies for complexes with Ce^{3+} ions in solution (1145 cm^{-1}) and at the bastnäsite surface (1150 cm^{-1}), which is fully consistent with the model DFT calculations predicting a shift in the ester C−O stretch from 1123 to 1135 cm^{-1} upon complexation. A broad band for a free ligand corresponding to the N−O stretch and the aromatic C−H in-plane bending is at ∼1030 cm^{-1}. The increased frequency of this band with aqueous Ce^{3+} (1056 cm^{-1}) and in the presence of bastnäsite (1063 cm^{-1}) is consistent with complex formation. DFT calculations were used to support this assignment and confirm the increased frequency of this band (by 20 cm^{-1}) going from a deprotonated L_4' ligand to a bidentate coordinated L_4'−Ce^{3+} complex.

Vibrational Sum Frequency Generation Studies. Vibrational sum frequency generation (vSFG) spectroscopy affords unique insights into the adsorption of ligands on the bastnäsite-[$10\bar{1}0$] surface, providing information related to ligand adsorption and surface orientation. Our attempts to obtain spectra for L_1 on the surface, however, revealed no reliable vibrational signatures despite our expectation of a strong signal due to C−H stretching modes from the nonplanar cyclohexane moiety. As a result, we suspect that L_1 does not adsorb strongly onto the surface. This result agrees with the relatively low adsorption energy based on DFT (Table 1) and the weak signals seen for the L_1—bastnäsite ATR-FTIR spectrum (Figure S3).

With DFT (Figure 3) and ATR-FTIR (Figure S4, vide infra) results showing substantial similarity in L_2 adsorption to that of SHA,[42] we proceed to our vSFG results for L_3 as plotted in Figure 6a for the SSP- and PPP-polarized spectra. The concentration-dependent integrated vSFG intensities plotted in Figure 6b were obtained in the SSP polarization combination and were fit to the Langmuir isotherm model of the form

$$I_{\mathrm{vSFG}}(C) = \left[\frac{(\alpha \cdot C \cdot K_{\mathrm{ads}})}{(1 + C \cdot K_{\mathrm{ads}})}\right]^2 \tag{3}$$

where α is an amplitude related to the maximum coverage, and C is the ligand concentration. The extracted equilibrium constant at 296 K was $K_{\mathrm{ads}} = 27.76 \pm 4.98$ mM^{-1}. This value is lower than that for SHA on the same surface[42] (i.e., 659 ± 134 mM^{-1}), indicating weaker adsorption in L_3, in agreement with DFT results in the presence of explicit water molecules (Table 1). Using the ratio of CH$_3$-asymmetric stretching amplitude measured in the PPP polarization combination (feature at ∼2975 cm^{-1}) to the CH$_3$ symmetric stretching mode (peak near 2875 cm^{-1}) measured in the SSP polarization combination, one can extract the average CH$_3$ tilt angle of 25.5° with respect to the surface normal (Figure 6c). Corresponding angles resulting from DFT calculations (Figures 3 and 4) are presented in Table 2. We find that the DFT treatment that explicitly includes solvent molecules provided good agreement for the L_3 orientation with respect to experiment and results in the correct trend for L_3 adsorption energy on bastnäsite-[$10\bar{1}0$] as compared to SHA.

Table 2. Orientation Angle and Reaction Energy of L_3 (Illustrated in Figure 6c) as Calculated from DFT with Implicit Solvation and in the Presence of Two Monolayers of Water

theoretical system	orientation angle	L_3 adsorption energy relative to SHA (kJ/mol)
no explicit water (Figure 3a)	61°	−12.9[a]
explicit water present (Figure 4a)	21°	+8.9[b]

[a] $E_{\mathrm{ads}}(L_3) - E_{\mathrm{ads}}(\mathrm{SHA})$, using E_{ads} from eq 1. [b] $E_{\mathrm{ads}}(L_3) - E_{\mathrm{ads}}(\mathrm{SHA})$, using E_{ads} from eq 2.

Raman Spectroscopy Studies. Raman spectra of L_1 and L_3 are shown in Figure S5 and show an absence of strong signals arising from ligand adsorption to bastnäsite, indicating either weak adsorption or a reduced Raman response due to the orientation of the molecules on the surfaces, in agreement with vSFG experiments. In contrast, the L_4' ligand shows a strong feature at 1495 cm^{-1} which resembles band position in BHA. To better visualize the difference between the pure surface of bastnäsite and the changes introduced by the ligand adsorption, the contribution from the bastnäsite itself was subtracted. This was done by normalizing the spectra to the characteristic peak at ∼1200 cm^{-1} that corresponds to the vibrations of carbonates in bastnäsite. The resulting crystal-subtracted spectrum, in addition to the spectrum of pure L_4', are presented in Figure 7.

Similar to BHA spectra, the band at 1495 cm^{-1} could be attributed to changes in the vibration of −C−N− or/and −C=O− bonds in hydroxamate as a result of the interaction of L_4' with the surface of the crystal. The exact assignment of this band is challenging. According to results of our DFT

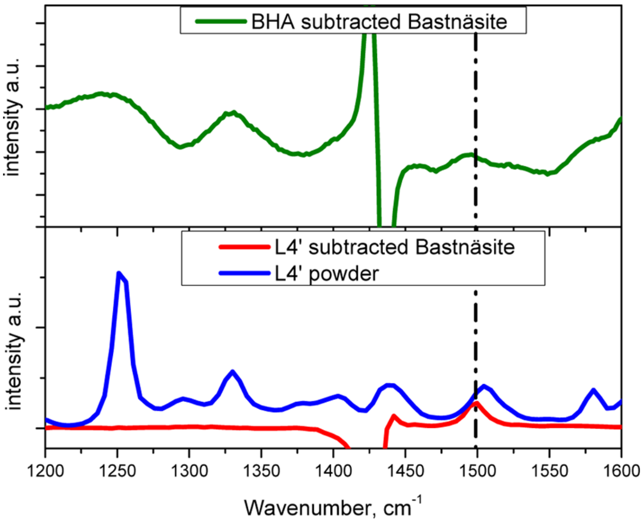

Figure 7. Raman spectra of pure L_4' (blue traces) and in the presence of bastnäsite (red traces), along with spectra of BHA in the presence of bastnäsite taken from ref 42.

calculations, one of the options is the interaction of both hydroxamic acid oxygen atoms with the bastnäsite surface to form a chelate ring structure. The appearance of new band at 1574 cm^{-1} in the FTIR spectrum of the absorbed L_4' could also be related to the changes in vibrational modes in hydroxamate moieties upon binding to metal surface. Another possibility is the shift of the C−N vibration stretch presented in the L_4' powder (Figure 7) from 1510 to 1495 cm^{-1} in the presence of bastnäsite.[71] To explore the nature of L_4' binding to bastnäsite further, we performed XPS measurements.

XPS Studies. The survey spectrum of the bastnäsite crystal (Figure S6) indicates a high content of carbon which is probably due to unavoidable sample handing. After treatment of the crystal with L_4', the C and N concentrations on bastnäsite increased from 46.4 to 87.8 at. % and from 0.35 to 0.9 at. %, respectively, while the Ce concentration decreased from 3.8 to 0.12 at. %, which suggested that the L_4' ligand adsorbed on the surface of the crystal. The high-resolution XPS of O 1s, N 1s, and Ce 3d for L_4', bastnäsite + L_4', and polished bastnäsite are presented in Figure 8. The O 1s XPS spectra of bastnäsite shows one well defined peak at ∼531.4 eV that is attributed to carbonate. Notably, the L_4' powder spectrum was composed of two peaks. The one that appeared at ∼532.8 eV that was assigned to both O−C and O−N species, while peak at 531.1 eV was assigned to O═C. After reaction of L_4' with bastnäsite, the spectrum contained three well defined peaks at 533, 531.5, and 529.4 eV. The band at 533 eV was assigned to the O−C band. The peak at 531.5 eV was assigned to both O−N and C═O bands. The absence of a separate peak related to the O−N band in the spectrum of bastnäsite + L_4 suggests that two O atoms in the hydroxamate group exist in a uniform chemical environment and have similar electron configurations. According to ref 72, it is possible that similarity in the local chemical environment can arise from the formation of a five-

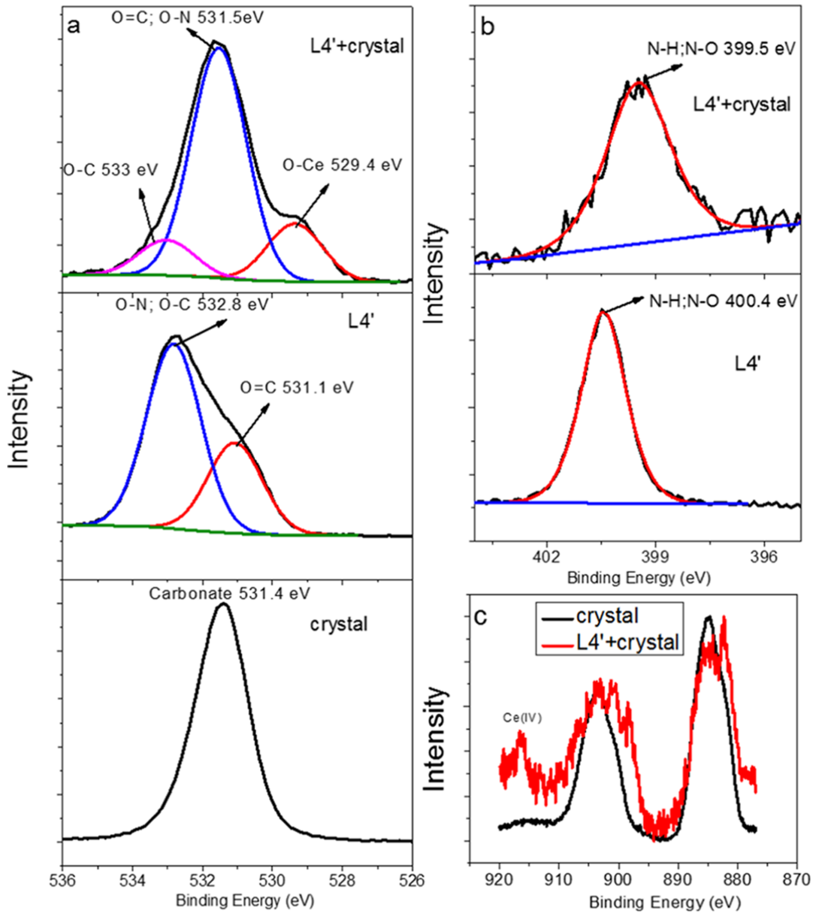

Figure 8. XPS spectra with peak fitting assignment of crystal + L_4', L_4', and polished crystal presented for O 1s (a), N 1s (b), and Ce 3d (c).

membered chelate ring (e.g., bidentate −O−Ce−O−N−C− chelation) formed on the surface of the crystal. Furthermore, an additional peak at 529.4 eV was related to O−Ce. Because this band is absent in the spectra of polished bastnäsite, the oxygen(s) in the ligand directly bind to Ce ions on the surface of crystal. The −O−C− band in O 1s XPS shows an increase in electron density in respect to pure L_4' which implies that the oxygen share H with the surface by forming hydrogen bonds with metal oxide or/and surface fluorine, which is in agreement with our DFT work.

The N 1s spectrum of L_4' contains only one peak at 400.4 eV that is associated with the N atom in the hydroxamate moiety. After L_4' adsorbed to the crystal, the binding energy decreased to 399.5 eV, suggesting a decrease in the electron density which could be due, for example, a coordinate bond to the Ce^{3+} ion involving the hydroxamate oxygen atom. While Ce 3d spectra are difficult to interpret, the qualitative evaluation suggests changes in the spectral shape of Ce 3d after ligand adsorption. In addition, a characteristic band of Ce^{4+} is present in the spectra of the adsorbed ligand. The results of XPS support chemisorption of the ligand on the surface of bastnäsite and strong binding of the ligand through hydroxamate groups directly to the Ce^{3+} ions.

■ CONCLUSIONS

Using a combined theoretical and spectroscopic approach, we probed the adsorption of five hydroxamic acid ligands onto the surfaces of REE-containing bastnäsite and calcite, a gangue mineral present in REE-containing ores. The consideration of adsorption in both the presence and absence of explicit solvent water molecules in DFT calculations provided new and important insights into the interplay between intra-ligand interactions and mineral adsorption. Theoretical analysis also helped to expose some of the deficiencies of the implicit solvent model and the Grimme's D3 treatment when applied to mineral surfaces. Specifically, L_3 is predicted to adsorb more strongly than SHA, but the ATF-FTIR, vSFG, and Raman data indicate the opposite. Therefore, we conclude that employing a purely implicit solvent model that lacks specific interactions between the solvent molecules and adsorbates on the mineral surface precludes accurate estimation of adsorption energies. These shortcomings are overcome by including two monolayers of explicit water molecules.

Water molecules, when treated explicitly in our DFT calculations, serve to stabilize the adsorption of all ligands probed on the bastnäsite-$[10\bar{1}0]$ and calcite-$[10\bar{1}4]$ surfaces, albeit to varying degrees depending on the extent of interaction with the surface and solvent, as well as intramolecular hydrogen bonding. Interestingly, the interplay of these factors integrally shifts due to explicit solvation, disfavoring bastnäsite adsorption in the absence of explicit water molecules of those adsorbates that exhibit intramolecular hydrogen bonding while enhancing adsorption when explicit solvent is present. The molecular flexibility otherwise precluded by the intramolecular hydrogen bond allows for the presence of water between adsorbed ligands and the bastnäsite surface, weakening adsorption in those ligands in which the hydrogen bond is not possible. Experimental spectra support weak adsorption of L_1 onto bastnäsite and similar adsorption modes between SHA and L_2. Vibrational sum frequency generation results for L_3 show the best agreement with DFT systems in which the solvent is explicitly included, highlighting a necessity for explicit solvation to correctly predict the orientation angle and a relative affinity to the surface in comparison with SHA. Shorter spacing between metal cations on the calcite-$[10\bar{1}4]$ surface results in the presentation of hydrophobic moieties into the solvent medium. There exists an optimal degree of hydrophobicity for calcite adsorption, wherein the inclusion of a second hydroxamic acid group (L_4) relative to SHA results in weaker adsorption, but also the removal of the phenolic group (BHA) or inclusion of a methyl group (L_3) yield weaker adsorption.

Of the new ligands considered in this study, di-hydroxamic acid L_4 adsorbs the most strongly on the explicitly solvated bastnäsite surface and also shows the greatest difference in adsorption energy across the lowest-energy explicitly solvated bastnäsite and calcite. Thus, considering the necessary inclusion of water in the froth flotation process, our calculations predict promising beneficiation efficacy with L_4 based on ligand adsorption studies. While several attempts to prepare L_4 were unsuccessful, a ligand L_4' in which one hydroxamic moiety is substituted by an ester group has been shown spectroscopically to chemisorb to the bastnäsite-$[10\bar{1}0]$ surface and, thus, is also expected to incite a strong flotation response. This is supported by DFT calculations, which also show a large difference in adsorption energies between bastnäsite and calcite with bastnäsite being favored.

We anticipate that our approach, developed to relate fundamentally the structures of adsorbates and mineral surfaces to adsorption energies and coupled with spectroscopic characterization using various surface-sensitive techniques, provides meaningful insights into molecular recognition in these systems and the design of future ligands for REE beneficiation via froth flotation.

■ ASSOCIATED CONTENT

Supporting Information

The Supporting Information is available free of charge at https://pubs.acs.org/doi/10.1021/acs.langmuir.1c03422.

> DFT-optimized interatomic distances; structure of the adsorbed water on mineral surfaces in the absence of any collector; collector synthesis; additional ATR-FTIR, Raman, and XPS spectra of adsorbed collectors; and NMR spectra of the synthesized compounds (PDF)

■ AUTHOR INFORMATION

Corresponding Authors

Vera Bocharova − *Chemical Sciences Division, Oak Ridge National Laboratory, Oak Ridge, Tennessee 37831, United States;* orcid.org/0000-0003-4270-3866; Phone: (865) 576-6490; Email: bocharovav@ornl.gov

Benjamin Doughty − *Chemical Sciences Division, Oak Ridge National Laboratory, Oak Ridge, Tennessee 37831, United States;* orcid.org/0000-0001-6429-9329; Phone: (865) 574-8955; Email: doughtybl@ornl.gov

Vyacheslav S. Bryantsev − *Chemical Sciences Division, Oak Ridge National Laboratory, Oak Ridge, Tennessee 37831, United States;* orcid.org/0000-0002-6501-6594; Phone: (865) 576-4272; Email: bryantsevv@ornl.gov; Fax: (865) 576-7956

Authors

Robert C. Chapleski, Jr. − *Chemical Sciences Division, Oak Ridge National Laboratory, Oak Ridge, Tennessee 37831, United States*

Azhad U. Chowdhury − *Chemical Sciences Division, Oak Ridge National Laboratory, Oak Ridge, Tennessee 37831, United States;* orcid.org/0000-0002-6735-815X
Anna K. Wanhala − *Chemical Sciences Division, Oak Ridge National Laboratory, Oak Ridge, Tennessee 37831, United States*
Luke D. Gibson − *Computational Sciences and Engineering Division, Oak Ridge National Laboratory, Oak Ridge, Tennessee 37831, United States;* orcid.org/0000-0002-8696-1878
Dīāna Stamberga − *Chemical Sciences Division, Oak Ridge National Laboratory, Oak Ridge, Tennessee 37831, United States;* orcid.org/0000-0002-6336-3402
Santa Jansone-Popova − *Chemical Sciences Division, Oak Ridge National Laboratory, Oak Ridge, Tennessee 37831, United States;* orcid.org/0000-0002-0690-5957
Robert L. Sacci − *Chemical Sciences Division, Oak Ridge National Laboratory, Oak Ridge, Tennessee 37831, United States;* orcid.org/0000-0002-0073-5221
Harry M. Meyer, III − *Chemical Sciences Division, Oak Ridge National Laboratory, Oak Ridge, Tennessee 37831, United States*
Andrew G. Stack − *Chemical Sciences Division, Oak Ridge National Laboratory, Oak Ridge, Tennessee 37831, United States;* orcid.org/0000-0003-4355-3679

Complete contact information is available at:
https://pubs.acs.org/10.1021/acs.langmuir.1c03422

Notes

The authors declare no competing financial interest.

■ ACKNOWLEDGMENTS

This research was supported by the Critical Materials Institute, an Energy Innovation Hub funded by the US Department of Energy, Office of Energy Efficiency and Renewable Energy, Advanced Manufacturing Office. This research used resources of the National Energy Research Scientific Computing Center (NERSC), a US Department of Energy Office of Science User Facility operated under contract no. DE-AC02-05CH11231. We are grateful to Alexandra Navrotsky at Arizona State University for providing synthetic bastnäsite samples. Notice: this paper has been authored by UT-Battelle, LLC, under contract DE-AC05-00OR22725 with the US Department of Energy (DOE). The US government retains and the publisher, by accepting the article for publication, acknowledges that the US government retains a nonexclusive, paid-up, irrevocable, worldwide license to publish or reproduce the published form of this paper, or allow others to do so, for US government purposes. DOE will provide public access to these results of federally sponsored research in accordance with the DOE Public Access Plan (http://energy.gov/downloads/doe-public-access-plan).

■ REFERENCES

(1) Eggert, R.; Wadia, C.; Anderson, C.; Bauer, D.; Fields, F.; Meinert, L.; Taylor, P. Rare Earths: Market Disruption, Innovation, and Global Supply Chains. *Annu. Rev. Environ. Resour.* **2016**, *41*, 199−222.

(2) Ganguli, R.; Cook, D. R. Rare earths: A review of the landscape. *MRS Energy Sustain.* **2018**, *5*, 6.

(3) Jordens, A.; Cheng, Y. P.; Waters, K. E. A review of the beneficiation of rare earth element bearing minerals. *Miner. Eng.* **2013**, *41*, 97−114.

(4) Tunsu, C.; Petranikova, M.; Gergorić, M.; Ekberg, C.; Retegan, T. Reclaiming rare earth elements from end-of-life products: A review of the perspectives for urban mining using hydrometallurgical unit operations. *Hydrometallurgy* **2015**, *156*, 239−258.

(5) Carmichael, R. S. *Practical Handbook of Physical Properties of Rocks and Minerals (1988)*; CRC press, 2017.

(6) Bodek, I. *Environmental Inorganic Chemistry*; Pergamon press, 1988.

(7) Castor, S. B. The Mountain Pass rare-earth carbonatite and associated ultrapotassic rocks, California. *Can. Mineral.* **2008**, *46*, 779−806.

(8) Drew, L. J.; Qingrun, M.; Weijun, S. The Bayan Obo iron-rare-earth-niobium deposits, Inner Mongolia, China. *Lithos* **1990**, *26*, 43−65.

(9) Kynicky, J.; Smith, M. P.; Xu, C. Diversity of Rare Earth Deposits: The Key Example of China. *Elements* **2012**, *8*, 361−367.

(10) Mariano, A. N.; Mariano, A., Jr. Rare Earth Mining and Exploration in North America. *Elements* **2012**, *8*, 369−376.

(11) Yang, K.-F.; Fan, H.-R.; Santosh, M.; Hu, F.-F.; Wang, K.-Y. Mesoproterozoic carbonatitic magmatism in the Bayan Obo deposit, Inner Mongolia, North China: Constraints for the mechanism of super accumulation of rare earth elements. *Ore Geol. Rev.* **2011**, *40*, 122−131.

(12) Assis, S. M.; Montenegro, L. C. M.; Peres, A. E. C. Utilisation of hydroxamates in minerals froth flotation. *Miner. Eng.* **1996**, *9*, 103−114.

(13) Nagaraj, D. R. Process for improved precious metals recovery from ores with the use of alkylhydroxamate collectors. U.S. Patent 5,126,038 A, 1992.

(14) Yoon, R.-h.; Hilderbrand, T. M. Purification of kaolin clay by froth flotation using hydroxamate collectors. GB 2167687 A1, 1986.

(15) Cui, H.; Anderson, C. G. Alternative flowsheet for rare earth beneficiation of Bear Lodge ore. *Miner. Eng.* **2017**, *110*, 166−178.

(16) Liu, W.; Wang, X.; Miller, J. D. Collector Chemistry for Bastnaesite Flotation − Recent Developments. *Miner. Process. Extr. Metall. Rev.* **2019**, *40*, 370−379.

(17) Pradip; Fuerstenau, D. W. Design and development of novel flotation reagents for the beneficiation of Mountain Pass rare-earth ore. *Min. Metall. Explor.* **2013**, *30*, 1−9.

(18) Wanhala, A. K.; Doughty, B.; Bryantsev, V. S.; Wu, L.; Mahurin, S. M.; Jansone-Popova, S.; Cheshire, M. C.; Navrotsky, A.; Stack, A. G. Adsorption mechanism of alkyl hydroxamic acid onto bastnäsite: Fundamental steps toward rational collector design for rare earth elements. *J. Colloid Interface Sci.* **2019**, *553*, 210−219.

(19) Zhang, X.; Du, H.; Wang, X.; Miller, J. D. Surface chemistry aspects of bastnaesite flotation with octyl hydroxamate. *Int. J. Miner. Process.* **2014**, *133*, 29−38.

(20) Nagaraj, D. R.; Farinato, R. S. Evolution of flotation chemistry and chemicals: A century of innovations and the lingering challenges. *Miner. Eng.* **2016**, *96*−*97*, 2−14.

(21) Peiró, L. T.; Méndez, G. V. Material and Energy Requirement for Rare Earth Production. *JOM* **2013**, *65*, 1327−1340.

(22) Woodcock, J. T.; Sparrow, G. J.; Bruckard, W. J.; Johnson, N. W.; Dunne, R. Plant Practice: Sulfide Minerals and Precious Metals. In *"Froth Flotation, A Century of Innovation"*; Fuerstenau, M. C., Jameson, G., Yoon, R.-H., Eds.; Society for Mining, Metallurgy and Exploration, Inc.: Littleton, Colorado, 2007.

(23) Anderson, C. D. *Improved Understanding of Rare Earth Surface Chemistry and Its Application to Froth Flotation*; Colorado School of Mines, Arthur Lakes Library, 2015.

(24) Cao, Z.; Cao, Y.; Qu, Q.; Zhang, J.; Mu, Y. Separation of bastnäsite from fluorite using ethylenediamine tetraacetic acid as depressant. *Miner. Eng.* **2019**, *134*, 134−141.

(25) Marion, C.; Li, R.; Waters, K. E. A review of reagents applied to rare-earth mineral flotation. *Adv. Colloid Interface Sci.* **2020**, *279*, 102142.

(26) Nagaraj, D. R. The chemistry and application of chelating or complexing agents in minerals separations. *Reagents in Mineral Technology*; Routledge, 2018; pp 257−334.

(27) Pradip; Fuerstenau, D. W. The adsorption of hydroxamate on semi-soluble minerals. Part I: Adsorption on barite, Calcite and Bastnaesite. *Colloids Surf.* **1983**, *8*, 103−119.

(28) Pradip; Fuerstenau, D. W. Adsorption of hydroxamate collectors on semisoluble minerals Part II: Effect of temperature on adsorption. *Colloids Surf.* **1985**, *15*, 137−146.

(29) Xiong, W.; Deng, J.; Zhao, K.; Wang, W.; Wang, Y.; Wei, D. Bastnaesite, Barite, and Calcite Flotation Behaviors with Salicylhydroxamic Acid as the Collector. *Minerals* **2020**, *10*, 282.

(30) Espiritu, E. R. L.; da Silva, G. R.; Azizi, D.; Larachi, F.; Waters, K. E. The effect of dissolved mineral species on bastnäsite, monazite and dolomite flotation using benzohydroxamate collector. *Colloids and Surfaces, A: Physicochemical and Engineering Aspects* **2018**, *539*, 319−334.

(31) Yang, Z.; Wu, W.; Bian, X. Synthesis of 3-hydroxy-2-naphthyl hydroxamic acid collector: flotation performance and adsorption mechanism on bastnaesite. *J. South. Afr. Inst. Min. Metall.* **2017**, *117*, 593−598.

(32) Duan, H.; Liu, W.; Wang, X.; Liu, W.; Zhang, N.; Zhou, S. Flotation separation of bastnaesite from calcite using novel octylmalon dihydroxamic acid as collector. *J. Mol. Liq.* **2020**, *312*, 113484.

(33) Cao, S.; Cao, Y.; Liao, Y.; Ma, Z. Depression mechanism of strontium ions in bastnaesite flotation with salicylhydroxamic acid as collector. *Minerals* **2018**, *8*, 66.

(34) Li, M.; Gao, K.; Zhang, D.; Duan, H.; Ma, L.; Huang, L. The influence of temperature on rare earth flotation with naphthyl hydroxamic acid. *J. Rare Earths* **2018**, *36*, 99−107.

(35) Foucaud, Y.; Badawi, M.; Filippov, L.; Filippova, I.; Lebègue, S. A review of atomistic simulation methods for surface physical-chemistry phenomena applied to froth flotation. *Miner. Eng.* **2019**, *143*, 106020.

(36) Elam, W. A. Molecular Modeling for the Design of Novel Performance Chemicals and Materials. *Yale J. Biol. Med.* **2014**, *87*, 604−605.

(37) Pradip. Design of crystal structure-specific surfactants based on molecular recognition at mineral surfaces. *Curr. Sci.* **1992**, *63*, 180−186.

(38) Pradip; Rai, B. Molecular modeling and rational design of flotation reagents. *Int. J. Miner. Process.* **2003**, *72*, 95−110.

(39) Pradip; Rai, B.; Rao, T. K.; Krishnamurthy, S.; Vetrivel, R.; Mielczarski, J.; Cases, J. M. Molecular Modeling of Interactions of Diphosphonic Acid Based Surfactants with Calcium Minerals. *Langmuir* **2002**, *18*, 932−940.

(40) Srinivasan, S. G.; Shivaramaiah, R.; Kent, P. R. C.; Stack, A. G.; Riman, R.; Anderko, A.; Navrotsky, A.; Bryantsev, V. S. A comparative study of surface energies and water adsorption on Ce-bastnäsite, La-bastnäsite, and calcite via density functional theory and water adsorption calorimetry. *Phys. Chem. Chem. Phys.* **2017**, *19*, 7820−7832.

(41) Srinivasan, S. G.; Shivaramaiah, R.; Kent, P. R. C.; Stack, A. G.; Navrotsky, A.; Riman, R.; Anderko, A.; Bryantsev, V. S. Crystal Structures, Surface Stability, and Water Adsorption Energies of La-Bastnäsite via Density Functional Theory and Experimental Studies. *J. Phys. Chem. C* **2016**, *120*, 16767−16781.

(42) Chapleski, R. C.; Chowdhury, A. U.; Wanhala, A. K.; Bocharova, V.; Roy, S.; Keller, P. C.; Everly, D.; Jansone-Popova, S.; Kisliuk, A.; Sacci, R. L.; Stack, A. G.; Anderson, C. G.; Doughty, B.; Bryantsev, V. S. A Molecular-Scale Approach to Rare-Earth Beneficiation: Thinking Small to Avoid Large Losses. *iScience* **2020**, *23*, 101435.

(43) Everly, D. Surface Chemistry of Novel Collectors and their Application to Froth Flotation of Rare Earth Minerals. M.Sc Thesis, Colorado School of Mines, Golden, CO, USA, 2017.

(44) Everly, D.; Anderson, C.; Jansone-Popova, S.; Bryantsev, V.; Moyer, B. A. *Flotation of Bastnaesite Ore Using Novel Collectors*; Oak Ridge National Lab. (ORNL): Oak Ridge, TN, United States, 2020.

(45) Kresse, G.; Furthmüller, J. Efficiency of ab-initio total energy calculations for metals and semiconductors using a plane-wave basis set. *Comput. Mater. Sci.* **1996**, *6*, 15−50.

(46) Kresse, G.; Furthmüller, J. Efficient iterative schemes for ab initio total-energy calculations using a plane-wave basis set. *Phys. Rev. B: Condens. Matter Mater. Phys.* **1996**, *54*, 11169−11186.

(47) Kresse, G.; Hafner, J. Ab initio molecular dynamics for liquid metals. *Phys. Rev. B: Condens. Matter Mater. Phys.* **1993**, *47*, 558−561.

(48) Kresse, G.; Hafner, J. Ab initio molecular-dynamics simulation of the liquid-metal-amorphous-semiconductor transition in germanium. *Phys. Rev. B: Condens. Matter Mater. Phys.* **1994**, *49*, 14251−14269.

(49) Blöchl, P. E. Projector augmented-wave method. *Phys. Rev. B: Condens. Matter Mater. Phys.* **1994**, *50*, 17953−17979.

(50) Kresse, G.; Joubert, D. From ultrasoft pseudopotentials to the projector augmented-wave method. *Phys. Rev. B: Condens. Matter Mater. Phys.* **1999**, *59*, 1758−1775.

(51) Perdew, J. P.; Burke, K.; Ernzerhof, M. Generalized Gradient Approximation Made Simple. *Phys. Rev. Lett.* **1996**, *77*, 3865−3868.

(52) Perdew, J. P.; Burke, K.; Ernzerhof, M. Generalized Gradient Approximation Made Simple [Phys. Rev. Lett. 77, 3865 (1996)]. *Phys. Rev. Lett.* **1997**, *78*, 1396.

(53) Grimme, S.; Antony, J.; Ehrlich, S.; Krieg, H. A consistent and accurate ab initio parametrization of density functional dispersion correction (DFT-D) for the 94 elements H-Pu. *J. Chem. Phys.* **2010**, *132*, 154104.

(54) Fishman, M.; Zhuang, H. L.; Mathew, K.; Dirschka, W.; Hennig, R. G. Accuracy of exchange-correlation functionals and effect of solvation on the surface energy of copper. *Phys. Rev. B: Condens. Matter Mater. Phys.* **2013**, *87*, 245402.

(55) Mathew, K.; Sundararaman, R.; Letchworth-Weaver, K.; Arias, T. A.; Hennig, R. G. Implicit solvation model for density-functional study of nanocrystal surfaces and reaction pathways. *J. Chem. Phys.* **2014**, *140*, 084106.

(56) Frenkel, D.; Smit, B. *Understanding Molecular Simulation: from Algorithms to Applications*; Elsevier, 2001; Vol. *1*.

(57) Hoover, W. G. Canonical dynamics: Equilibrium phase-space distributions. *Phys. Rev. A: At., Mol., Opt. Phys.* **1985**, *31*, 1695−1697.

(58) Nosé, S. A unified formulation of the constant temperature molecular dynamics methods. *J. Chem. Phys.* **1984**, *81*, 511−519.

(59) Nosé, S. Constant Temperature Molecular Dynamics Methods. *Prog. Theor. Phys.* **1991**, *103*, 1−46.

(60) Frisch, M. J.; Trucks, G. W.; Schlegel, H. B.; Scuseria, G. E.; Robb, M. A.; Cheeseman, J. R.; Scalmani, G.; Barone, V.; Petersson, G. A.; Nakatsuji, H.; et al. *Gaussian 16*, Revision A. 03; Gaussian, Inc.: Wallingford, CT, 2016.

(61) Coucouvanis, D. Syntheses of Selected Supramolecules. *Inorganic Syntheses*; John Wiley & Sons, Ltd, 2002; pp 1−74.

(62) Ghosh, H.; Patel, B. K. Hypervalent Iodine(III)-Mediated Oxidation of Aldoximes to N-Acetoxy or N-Hydroxy Amides. *Org. Biomol. Chem.* **2010**, *8*, 384−390.

(63) Martínez-Aguirre, M. A.; Flores-Alamo, M.; Yatsimirsky, A. K. Thermodynamic and structural study of complexation of phenylboronic acid with salicylhydroxamic acid and related ligands. *Appl. Organomet. Chem.* **2018**, *32*, No. e4405.

(64) Geffken, D. Zur Cyclisierung von Salicylsäureamiden und Salicylohydroxamsäuren mit 1,1′-Carbonyldiimidazol. *Liebigs Ann. Chem.* **1981**, *1981*, 1513−1514.

(65) Chowdhury, A. U.; Liu, F.; Watson, B. R.; Ashkar, R.; Katsaras, J.; Collier, C. P.; Lutterman, D. A.; Ma, Y.-Z.; Calhoun, T. R.; Doughty, B. Flexible approach to vibrational sum-frequency generation using shaped near-infrared light. *Opt Lett.* **2018**, *43*, 2038−2041.

(66) Chowdhury, A. U.; Watson, B. R.; Ma, Y.-Z.; Sacci, R. L.; Lutterman, D. A.; Calhoun, T. R.; Doughty, B. A new approach to vibrational sum frequency generation spectroscopy using near infrared pulse shaping. *Rev. Sci. Instrum.* **2019**, *90*, 033106.

(67) Adams, E. M.; Verreault, D.; Jayarathne, T.; Cochran, R. E.; Stone, E. A.; Allen, H. C. Surface organization of a DPPC monolayer

on concentrated $SrCl_2$ and $ZnCl_2$ solutions. *Phys. Chem. Chem. Phys.* **2016**, *18*, 32345−32357.

(68) Chowdhury, A. U.; Lin, L.; Doughty, B. Hydrogen-Bond-Driven Chemical Separations: Elucidating the Interfacial Steps of Self-Assembly in Solvent Extraction. *ACS Appl. Mater. Interfaces* **2020**, *12*, 32119−32130.

(69) Cutini, M.; Maschio, L.; Ugliengo, P. Exfoliation Energy of Layered Materials by DFT-D: Beware of Dispersion! *J. Chem. Theory Comput.* **2020**, *16*, 5244−5252.

(70) Klimeš, J.; Bowler, D. R.; Michaelides, A. Chemical accuracy for the van der Waals density functional. *J. Phys.: Condens. Matter* **2010**, *22*, 022201.

(71) Adiguzel, E.; Yilmaz, F.; Emirik, M.; Ozil, M. Synthesis and characterization of two new hydroxamic acids derivatives and their metal complexes. An investigation on the keto/enol, E/Z and hydroxamate/hydroximate forms. *J. Mol. Struct.* **2017**, *1127*, 403−412.

(72) Qi, J.; Liu, G.; Dong, Y. Probing the hydrophobic mechanism of N-[(3-hydroxyamino)-propoxy]-N-octyl dithiocarbamate toward bastnaesite flotation by in situ AFM, FTIR and XPS. *J. Colloid Interface Sci.* **2020**, *572*, 179−189.